# Embedded Effective-Index-Material in Oxide-Free Hybrid Silicon Photonics Characterized by Prism Deviation

Kristelle Bougot-Robin, C. Pang, Xavier Pommarede, A. Itawi, Anne Talneau, Jean-Paul Hugonin, Henri Benisty

# Embedded Effective-Index-Material in Oxide-Free Hybrid Silicon Photonics Characterized by Prism Deviation

K. Bougot-Robin, C. Pang, X. Pommar`ede, A. Itawi, A. Talneau, J. P. Hugonin, and H. Benisty

***Abstract*—Hybrid silicon photonics offers novel opportunities to control light propagation with nanostructured media on the silicon side. In the specific case of oxide-free heteroepitaxial bonding of III-V layers on silicon, it is particularly crucial to assess the role of nanostructures in the post-bonding situation. We propose here a method of internal light source and integrated prism deviation to evaluate the effective index of small sub-wavelength periodic shallow holes that are completely embedded and do not lend themselves to alternative such as e.g. ellipsometry. We achieve a precision $\Delta n < 0.01$, a good accuracy both for the understanding and optimization of optical components performances. Measured data are in good agreement with the theoretical expectation, as obtained using an improved homogenization strategy and further confirmed by 3D Bloch mode calculation.**

***Index Terms*—Embedded effective medium, integrated optoelectronics, photoluminescence, prism deviation, waveguides.**

## I. Introduction

HYBRID silicon photonics combines the advantages of maturity and scales of silicon technologies (e.g. complementary metal–oxide–semiconductor) with III–V compounds functionalities. It opens new possibilities for integrated components and has gained increasing momentum in recent years [1].

Classically, integration of III-V materials on Si is realized by means of wafer bonding, using either an intermediate layer of polymer such as benzocyclobutene, or thick/thin oxide [2] with molecular bonding to accommodate lattice mismatch. This intermediate layer brings issue in terms of electrical conduction as well as thermal conduction. We recently demonstrated direct bonding of indium phosphide (InP) epilayers on silicon (Si) [3] within a fully oxide-free process. It is expected that such a process gives rise to new electro-optical devices such as laser diodes, or semiconductor optical amplifiers, combining both active and passive optical properties with heat sinking and electrical conduction advantages [4].

K. Bougot-Robin, C. Pang, J. P. Hugonin, and H. Benisty are with the Laboratoire Charles Fabry, Institut d'optique Graduate School, 91127 Palaiseau, France (e-mail: kristelle_robin@yahoo.fr; chengxin.pang@gmail.com; jean-paul.hugonin@institutoptique.fr; henri.benisty@institutoptique.fr).

X. Pommarède, A. Itawi, and A. Talneau are with the LPN, CNRS-LPN, 91460 Marcoussis, France (e-mail: xavier.pommarede@3-5lab.fr; ahmad.itawi@lpn.cnrs.fr; anne.talneau@lpn.cnrs.fr).

Optical properties of oxide-free bonded structures need to be revisited in comparison to usual structures including a low index separating layer between the SOI (silicon-on-insulator) platform and the III-V materials. Based on a stronger mastery of material properties, integrated structures can be better optimized, e.g., to implement demanding optical devices achieving good heat sinking from InP towards the silicon substrate.

For such realizations, a preferred embodiment of optical components involves nanostructured materials made of air holes in a silicon matrix, so as to finely carve passive optical properties in the more easily processed SOI wafer. Such nanostructured materials with sub-wavelength periodicity can for instance provide an adjustable refractive index material, desired for mastered evanescence of guided modes and possible evanescent coupling to adjacent structures (rings, guides, absorbers, etc.).

In this context, there is a need to qualify optical properties of embedded nanostructures, for which electronic microscope characterization (SEM) is not sufficient. Moreover, the complexities of guidance may depend critically on how the structure is visited by modes, giving an advantage to a measurement based on internal guided light [5]. Such issues can typically be addressed by a better knowledge of the effective index of guided modes visiting such nanostructures.

Our current motivation for the quest of such effective indices is to understand the use of such nanostructures for use as cladding in channel waveguides, ridge lasers and similar devices. Even though in such specific applications, the effective material in question is a low index one hosting the evanescent tails of useful modes, a safe way to assess its effective properties is to use it as an effective medium for propagation. In our particular case, we choose prism-type embedded structures to probe these effective materials in a propagation regime.

## II. Assessment of Embedded Nanopatterns

In the following, we denote the patterned region operating in the subwavelength regime as an EMT material, using the familiar acronym of "Effective-Medium Theory" to refer to the material in question. With respect to a top view, we shall call also "EMT" the regions where this EMT material is embedded, without extra ambiguity given the context.

Specifically, we present a technique to determine the effective index of modes in EMT regions of an oxide-free heteroepitaxial bonded hybrid III–V-on-silicon structure, by studying the deviation induced by embedded nanopatterned prisms of 10–30 $\mu$m typical dimensions. Note that such small sizes ($<20\lambda$) make an

index determination by ellipsometric methods nearly impossible. Also, a reflectivity assessment from top would be delicate, because the nanostructure is embedded (bonding may affect its details to a small degree, so a measurement prior to bonding is not ideal) and because the buried silica/silicon reflections are also greatly interfering and are awkward to fully master.

The knowledge of *group index* $\mathrm{n_g}$ in these guiding systems is also certainly of interest. For cw techniques, it involves a study of fringe spacing in a piece of known length and substantial reflectivity at its edges (see [5] and subsequent work of this author group). It will be seen that our reflectivity between EMT and the rest is weak and not adequate for this measurement. But ongoing measurements on cleaved passive samples could bring the information. Another possibility is to extract guided light with a weak grating at known angles, as said in a more explicit context in the conclusion.

The targeted nanopatterned EMT consist in array of holes in a silicon matrix, with different diameters and periodicity, fabricated into the upper part of a silicon layer in an SOI substrate. After nanopattern fabrication using electron beam lithography based process, an InP membrane including active luminescent Quantum Wells (QW) is directly bonded on the patterned SOI substrate. Its substrate holder is removed, leaving a thin III–V bonded membrane. The oxide-free process details have been described elsewhere [6]. The quality of the bonding interface was characterized by nanoindentation and revealed a relatively high surface bonding energy of 585 mJ/m$^2$, suitable for hybrid devices in common applications [7]. In Fig. 1(a) we give a generic representation of the section of a mode guided in an EMT region, illustrating our motivation of better assessment of guiding properties. The final multilayer bonded stack with layer refractive index and thicknesses are detailed in Fig. 1(b). Thicknesses have been determined through SEM characterization of cleaved structures.

Such effective medium layer may be exploited in various optical components such as laser or optical amplifier [8] for deterministic evanescent coupling to selective elements (rings [9]), an often awkward issue when using pure air or pure silica gaps as cladding between coupled elements. In Fig. 1(c), a typical SEM micrograph shows the vertical section of a silicon ridge channel clad by EMT material beneath a III-V bonded layer [10]. The top view of a nanopatterned prism layout is given in Fig. 1(d). It is akin to a sub-wavelength photonic crystal. A square lattice geometry is privileged to avoid unwanted larger periods on the prism edges. The prism hypotenuse itself follows a "low Miller index" cut of the lattice.

To investigate guiding properties of the EMT, we exploit QW photoluminescence (PL) and the power of the Internal Light Source (ILS) technique [5]. The ILS technique consists in using the spontaneous emission of the material as an internal point source of guided light and will be detailed in the next section. We illustrate in Fig. 1(e) the prism deviation *D* caused to a beam coming from the photoluminescent source spot. As an anticipation to what follows, we also indicate on the figure the virtual point source position of the deviated beam, which will be shifted by an amount $\Delta y_{\mathrm{spot}}$ related by the laws of geometric optics to the EMT prism effective refractive index

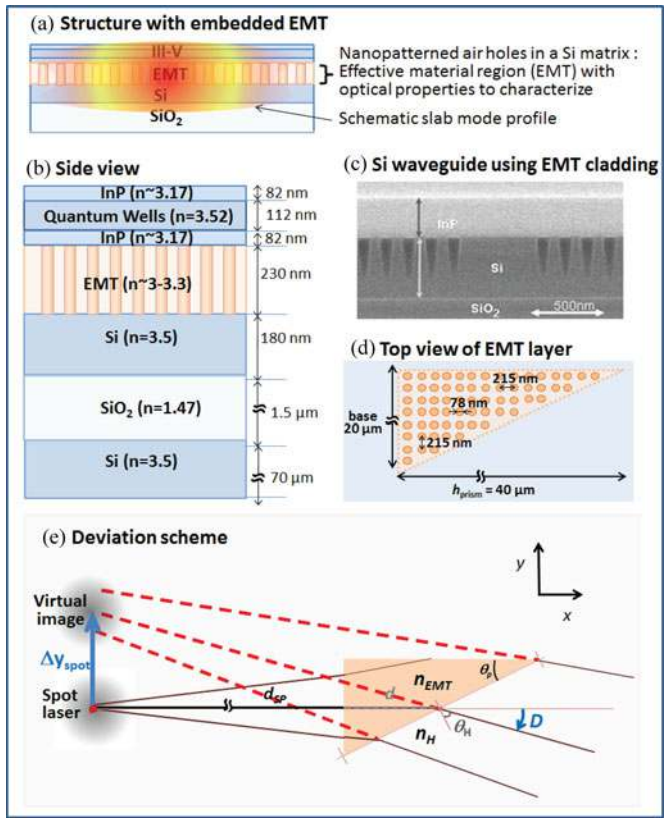


Fig. 1. (a) Guided mode in oxide-free structure involving effective material (air holes in silicon matrix). (b) Details of our fabricated structure. (c) Si ridge isolated in effective medium structure. (d) Deviating prisms details with air holes of ~80 nm diameter and ~200 nm center to center distance. (e) Deviation scheme using ILS technique.

and to the prism angle. Specifically, the beam deviation angle will be obtained through the apparent source shift $\Delta y_{\mathrm{spot}}$, and will allow to deduce the EMT effective index $n_{\mathrm{EMT}}$ relative to the surrounding hybrid stack mode effective index, denoted $n_H$, of the non-patterned region. The set-up and shift determination method using a cleaved edge are detailed in Section III.

## III. EMT Prism Deviation

### A. ILS Technique

To determine the deviation, we use the ILS technique and image both side emitted PL (excited at a distance $d_C$ from the cleaved edge) and front emitted PL, as sketched in Fig. 2. The scheme outlines the way the cleaved edge intervenes either for (a) light propagation without prism or (b) the prism induced deviation.

The guided light generated from a point source and emerging at a cleaved edge forms an astigmatic beam. The vertical wavefront diverges only at the cleaved edge, while for the in-plane beam wavefront, refraction causes the diffracted beam emerging toward the observer around normal incidence to stem from a virtual quasipoint source at a distance $d_C/n$ inside the sample. The important point is that the same is true in the presence of beam deviation from the diffracting lattice hence the apparent

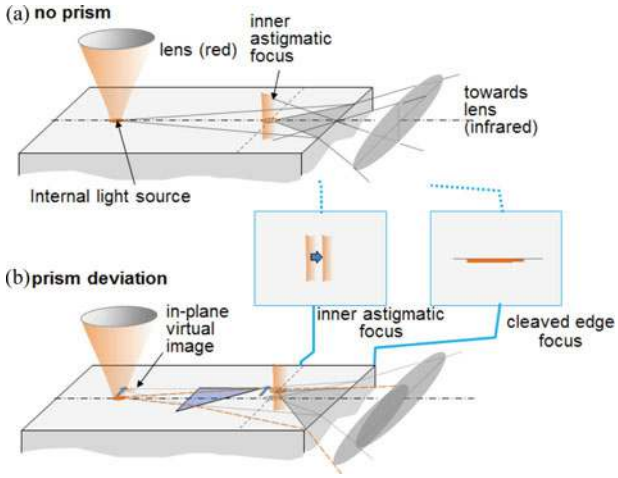


Fig. 2. Scheme of prism induced deviation with (a) beam in 3D without prism serving as reference and (b) beam in 3D with prism.

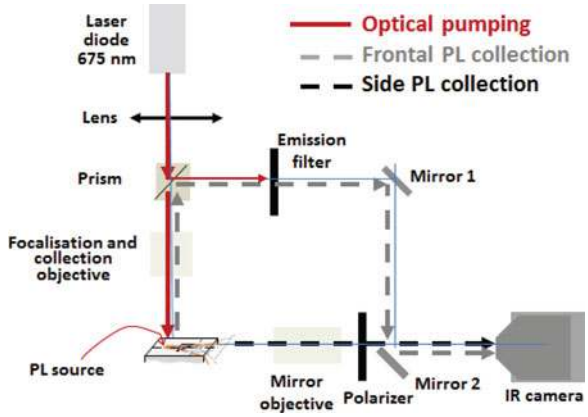


Fig. 3. Scheme of experimental setup for deviation measurement, with two collection channels for both front and lateral side emitted PL.

spot shift $\Delta y_{\rm spot}$ of Fig. 1(e) is also that of the quasi point source, for the reasonable apertures that we use (NA$\sim$0.4) [11]. By focusing away from the cleaved edge, one can actually find the focus of this virtual source: Due to refraction at the cleaved edge, it is seen at the distance $d_C/n$ mentioned above, but appears as a vertical bar rather than a point, due to the strong astigmatism of the wavefronts [12].

The ILS method can be used to determine the effective index of the EMT region. It allows different type of nanopatterned prisms (prism angles and prisms nanostructuration) to be measured without the coupling uncertainties of wafer-edge end-fire coupling [10].

### B. Prism Induced Deviation

Using Snell's law and Fig. 1(e) notations, we express the deviation *D* for single prisms of acute angle $\theta_P$ (or one half of the biprism detailed below), with index notations given above. For normal incidence angle, the deviation at the first interface is absent. With $n_{\rm EMT}$ the effective index of the guided wave in the EMT region, and $n_H$ the effective index of the guided wave out of the prism (no nanostructuration), the final deviation can be expressed as

$$n_{\rm EMT}\sin\left(\pi/2-\theta_P\right) \;=\; n_H\sin\theta_H \tag{1}$$

$$\theta_H \;=\; \sin^{-1}\left(\frac{n_{\rm EMT}}{n_H}\cos\theta_P\right) \tag{2}$$

$$D = \;\pi/2-\theta_H-\theta_P\,. \tag{3}$$

The distance between the source and the prism is noted as $d_{\rm SP}$, the distance in the prism as *d*. Thus, the spot deviation $\Delta y_{\rm spot}$ is given by

$$\Delta y_{\rm spot} = (d_{\rm SP}+d)\times\tan D \tag{4}$$

### C. Measurement Set-Up

In Fig. 3, we sketch the optics of the measurement set-up. Briefly, a laser diode of wavelength $\lambda = 675$ nm is focused on the sample to excite the PL which has an emission peak at $\lambda\sim$1530 nm. Using prism beam-splitters and on axis or slightly off-axis mirrors, both front and side emitted PL can be collected on the same infrared camera. We exploit both signals from the image, by taking care of using different parts of the detector array as much as possible (conversely, having coinciding patterns from both paths can help alignment and systematic measurements, but we shall not dive further in such details).

Our imaging setup provides a direct measure of the deviation of the source virtual image. We now show that it satisfactorily determines the mode effective index inside a prism for the TE polarization in this paper, and therefore helps characterizing the EMT guiding properties for TE modes. Work is in progress to assess the weak EMT birefringence (typically $[\Delta n_{\rm TE}-\Delta n_{\rm TM}]\sim<0.03$).

### D. Prisms Design

We designed single deviating prisms with rectangle base angle, as well as symmetric biprisms, deviating light symmetrically, as illustrated in Fig. 4(a). They all have a 20 $\mu$m base, and their heights are respectively 30 and 40 $\mu$m for rectangle prisms, and 10, 20 and 30 $\mu$m for biprisms. Prisms respective angles are of 33.7° and 26.57° for prisms, and 45°, 26.57°, and 18.43° for biprisms. To better fix ideas, with a subwavelength periodicity of $\sim$200 nm, a base of 20 $\mu$m corresponds to one hundred periods.

Light is incident perpendicularly to the prism base flat surface side, and undergoes its main large deviation on the second interface.

Two different EMT materials are studied. Holes diameters and etching depth are determined by SEM characterization. The etch depth in silicon is $\sim$230 nm. The first nanopattern structure has holes of diameters 74 nm, and a periodicity of 180 nm, while the second nanopattern structure has holes with diameters 78 nm and period of 215 nm. They are illustrated in Fig. 4(b). This corresponds to respective filling factors $f = 0.133$ and $f = 0.103$. At the wavelength $\lambda$ 1550 nm, the respective corresponding reduced frequencies are $u = \Lambda/\lambda = 0.116$ for $\Lambda = 180$ nm and $u = 0.1387$ for $\Lambda = 215$ nm. Both EMT types are fabricated in

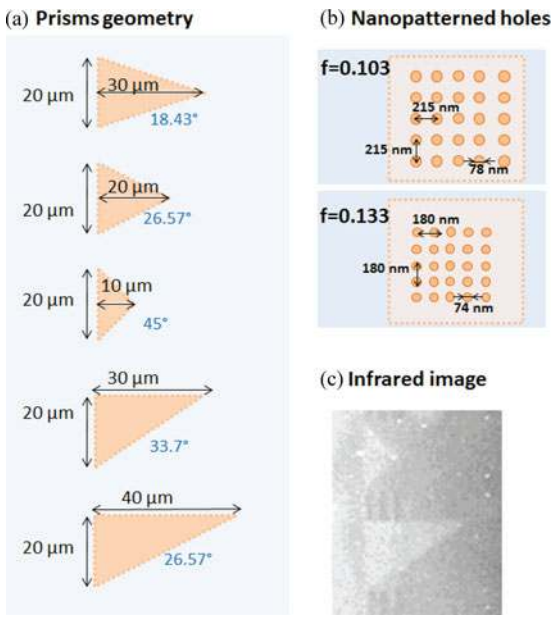


Fig. 4. (a) Prisms geometry. (b) Nanopatterns. (c) Infrared prisms image.

TABLE I
CALCULATED PRISM DEVIATIONS FOR $\Delta n = 0.35$

| Prism ($\mu$m) | $\theta_P$ (deg) | $D$ (deg) | $\Delta y_{spot}, \Delta n = 0.35$ ($\mu$m) |
|---|---|---|---|
| Prism $20 \times 30$ | 33.7 | 8.2 | **12.2** |
| Prism $20 \times 40$ | 26.6 | 10.3 | **16.3** |
| Biprism $10 \times 10$ | 45 | 5.7 | 8 |
| Biprism $10 \times 20$ | 26.6 | 10.3 | 16.3 |
| Biprism $10 \times 30$ | 18.4 | 13.5 | 23.9 |

the same run and within less than 200 $\mu$m from each other, so all other parameters (concerning sample fabrication and optical set-up adjustment) can be considered identical for comparison purpose. Fig. 4(c) gives an infrared picture of a prism adjacent to a biprism. The sample is illuminated by an infrared LED beam, and the chip further imaged by our camera detector.

For prism deviation measurements using ILS technique, the excitation source is placed on the entrance prism face axis. Thus, $d$ corresponds to the half-prism height $h_{\rm prism}/2$ for prisms, and to the prism height for biprisms $h_{\rm prism}$. To better fix ideas, we determined the deviations for a distance $d_{\rm SP} = 70$ $\mu$m, much larger than $d$.

The deviation angle and spot deviation given by (3) and (4) respectively are nearly linear functions of $\Delta n = n_{\rm H} - n_{\rm EMT}$. We thus report in Table I the calculated deviation corresponding to a maximal refractive index contrast $\Delta n = 0.35$ (our upper limit in change of refractive index). The calculation is made for a distance $d_{\rm SP} = 70$ $\mu$m (in line with the experiments presented in the following part). While the distance $d$ of various rays in the prism spans $[0 - h_{\rm prism}]$, we take its central value, namely $d = h_{\rm prism}/2$ and give the deviation estimates in Table I, both for prisms and biprisms.

Note that several issues complicate experimental deviation determination of biprisms. First, unlike the prism case, the source position does not correspond to the center of the face. Secondly, upper and lower deviations correspond to spots whose tails contributions overlap, thus modifying the maximum intensity position with respect to the underlying spot position. Therefore, in the experimental part, for index determination, only single prisms deviation will be used.

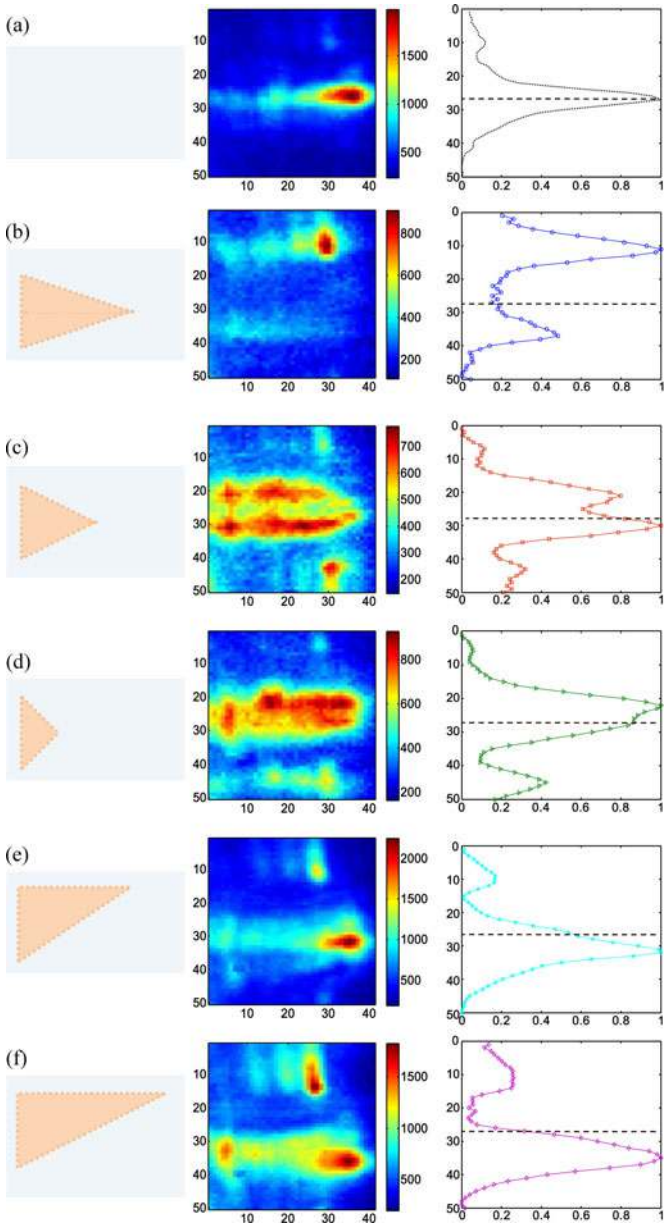


Fig. 5. Bare images (superposition of lateral and frontal PL emission images), zoomed image of the lateral photoluminescence) and averaged profile (a) for the reference (no nanostructured prism). (b) Biprism of base 20 $\mu$m and height 30 $\mu$m. (c) Biprism of base 20 $\mu$m and height 20 $\mu$m. (d) Biprism of base 20 $\mu$m and height 30 $\mu$m. (e) Biprisms of base 20 $\mu$m and height 30 $\mu$m. (f) Prism with base 20 $\mu$m and height 40 $\mu$m.

## IV. DEVIATION MEASUREMENTS

The deviations for the various single prisms and biprisms are reported in Fig. 5(a)–(f) with a scheme of the prism considered

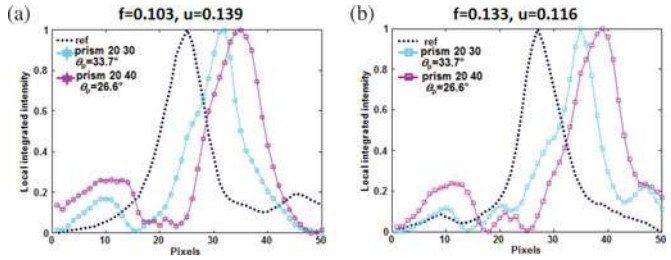


Fig. 6. Prisms deviation for single prisms (a) for filling factor of $f = 0.103$ and (b) for filling factor of $f = 0.133$.

TABLE II
MEASURED DEVIATION FOR DIFFERENT NANOSTRUCTURATIONS AND PRISMS

| **(a) f = 0.103, u = 0.139** | | | | **(b) f = 0.133, u = 0.116** | | | |
|---|---|---|---|---|---|---|---|
| $\theta_p$ | $\Delta y_{spot}$ (pixels) | $\Delta y_{spot}$ ($\mu$m) | $\Delta n$ | $\theta_p$ | $\Delta y_{spot}$ (pixels) | $\Delta y_{spot}$ ($\mu$m) | $\Delta n$ |
| 33.7° | 6.5 | 4.6 | $\mathbf{0.1245} \pm 0.020$ | 33.7° | 8 | 5.7 | $\mathbf{0.1556} \pm 0.020$ |
| 26.6° | 10 | 7.1 | $\mathbf{0.1408} \pm 0.015$ | 26.6° | 12 | 8.6 | $\mathbf{0.179} \pm 0.015$ |

in the first column. We report in the second column images for the prisms and biprisms with holes of diameter 78 nm and period 215 nm. The elongated bar is the result of astigmatism discussed in Section III.

From these images, we extract as well the profile over the *y*-direction, by averaging over the *x*-direction. These profiles are reported in the right column of Fig. 5.

For biprisms, from Fig. 5 (a)–(c) profiles, we confirm that spots are not well distinct. Moreover, it is less trivial to define the center of the spot, as the source is here aligned with the prism apex and not the center of the two constituting prisms faces. To obtain the EMT effective index $n_{\mathrm{EMT}}$ we thus rely on the deviation for the single prisms configuration, for the two types of fabricated nanopatterns, Fig. 5(e), (f). Profiles for both single prisms with same nanostructurations are reported in Fig. 6(a) for the filling factor $f = 0.103$ and (b) for the filling factor $f = 0.133$. The deviation is based on the position of the maximum of the profile, taken with a $\pm 0.5$ pixel accuracy. With a magnification of 1.4 pixels/$\mu$m, this corresponds to a $\pm 0.7$ $\mu$m accuracy, and therefore a precision in refractive index of $\Delta n = \pm 0.02$ for the single prism of height 30 $\mu$m, and $\Delta n = \pm 0.015$ for the prism of height 40 $\mu$m.

Other sources of errors come from the bonding and layer quality and imperfect optical alignment of the PL source spot with the center of the prism interface.

Deviation values $\Delta y_{\mathrm{spot}}$ are summarized in Table II, from which we extrapolate corresponding $\Delta n$ based on (4).

We also report the experimental values together with the calculated deviation curve in Fig. 7, where the error squares correspond to a position accuracy of 0.7 $\mu$m and we report vertically the resulting error in $\Delta n$ determination. The grey vertical bars give the interval of common determination. These bars correspond to the most reliable determination. For nanopattern of holes diameter 78 nm and period of 215 nm we obtain a TE index difference $\Delta n = n_H - n_{\mathrm{EMT}}$ spanning $\Delta n = [0.1258 - 0.1445] \sim 0.1351 \pm 0.0093$, and therefore, based on $n_H = 3.3156$, an index $n_{\mathrm{EMT}} = 3.1805$ for the filling factor of $f = 0.103$. For the EMT with holes diameter 74 nm and period 180 nm, we obtain a span $\Delta n = [0.1579 - 0.1756] \sim 0.1668 \pm 0.0088$, and therefore based again on $n_H = 3.3156$, an index $n_{\mathrm{EMT}} = 3.1488$ for the filling factor of $f = 0.133$. We thus obtain a $\Delta n$ determination with an error $\Delta n < 0.01$.

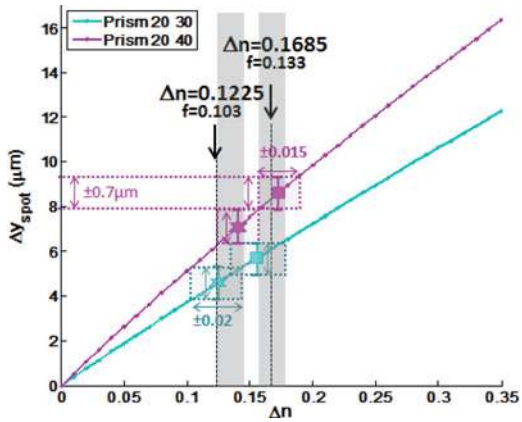


Fig. 7. Calculated deviation and experimental points with in square shape the nanopattern of filling factor $f = 0.103$ and in diamond shape the filling factor $f = 0.133$. The arrows point to the theortically calculated vlaues from the measured diameters.

We compare measured values to calculated values obtained through modeling of our structure (values corresponding to 3D Bloch mode calculation [13], [14] or obtained by a more intuitive homogenization strategy (HS) based on perturbation approach, as described in the Appendix). The calculated effective index difference are of $\Delta n = 0.1225$ for $f = 0.103$ at $u = 0.139$, and of $\Delta n = 0.1685$ for $f = 0.133$ at $u = 0.116$. They are reported in Fig. 7 by the two thick black arrows. There is a satisfying agreement with the experimental values, if we refer to the grey bars.

Of course, such modest discrepancies can also be partly accounted for by, e.g., the rounded shape of the hole bottom, (the period patterned by the e-beam equipment, on the other hand, is quite accurate). But overall, there is a fairly good degree of consistency.

## V. CONCLUSION

In this paper, we presented a new technique to assess the effective index of guided modes of small structures comprising embedded nanopatterns. Using the ILS Technique, we could determine the effective refractive index with a precision $\Delta n = \pm 0.009$. While precision could be further increased, the ILS technique provides a solution to determine refractive index where no alternative technique could be used. The measured values are in good agreement with theoretical expectation, as obtained with an improved HS and further confirmed with a 3D Bloch mode calculation.

The fabrication is demanding in the present first study because of the need for a cleaved edge. Nevertheless, this need could be alleviated using trenches to scatter light out.

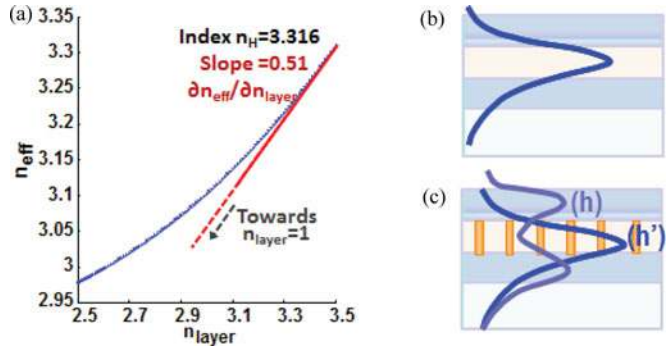


Fig. 8. (a) Effective index calculated with 1-D waveguide model as a function of $n_{\rm layer}$. (b) Mode profile without nanostructuration. (c) In the air holes, (h) and (h′) choices correspond to modified or "rigid" [same as (b)] field profiles.

TABLE III
EFFECTIVE INDEX VARIATION CALCULATED BY THE VARIOUS APPROACHES

| $(\mathbf{f},\mathbf{u})$ | $\mathbf{\Delta n(h\to v)}$ | $\mathbf{\Delta n(v\to h)}$ | $\mathbf{\Delta n(v'\to h)}$ | $\mathbf{\Delta n(3D)}$ |
|---|---|---|---|---|
| (0.103, 0.139) | 0.091 | 0.050 | 0.124 | 0.1225 |
| (0.133, 0.116) | 0.144 | 0.068 | 0.175 | 0.1685 |

Another caveat for the implementation of this technique is the possible advent of higher modes for thicker InP layers, that has to be carefully evaluated.

To further access to the dispersion inside prisms or along waveguides, an interesting possibility would be to include extra weakly scattering large-period gratings in the spirit of the work of Le Thomas *et al.* [15].

## APPENDIX

To determine the TE mode effective index in the patterned region, we seek HS. We shall extend our study elsewhere, but we discuss here the limitations of basic HS. We can classify HS as combinations of (h) horizontal and vertical (v) homogenizations. Horizontal homogenization exploits 2D photonic crystal band structure calculations based on plane wave expansion to get a phase index $n_\phi = \omega/k$, while vertical homogenization replaces the local vertical stack by its effective index $n_{\rm eff}$ (1D calculation). A good HS should fit a more sophisticated and less intuitive 3D Bloch mode calculation. We find, as detailed below, that neither (h $\to$ v) nor (v $\to$ h) are good HS for $\Delta n$, an unsatisfying situation given the novelty and possible importance of such structures (embedded holes in matrix in general). We propose a modified (v′ $\to$ h) HS that matches the exact 3D result well, where the vertical step (v′) privileges a perturbation approach.

Fig. 8 gives the TE effective index $n_{\rm eff}$ as a function of the index of a homogeneous EMT layer $n_{\rm layer}$ in the range [2.5–3.5].

In Table III, we summarize values obtained by the three HS (h $\to$ v),(v $\to$ h) and (v′ $\to$ h). The (h $\to$ v) HS first considers infinite holes in $n = 3.5$ matrix and then uses the obtained $n_\varphi$ value as $n_{\rm layer}$ for each of the two filling factors. This gives too high $n_{\rm eff}$ values, or equivalently too low $\Delta n$. This can be explained by the bandgap proximity especially at u = 0.1387, raising $n_\varphi$. The actual 3D wave will not be so close. The (v $\to$ h) HS considers the effective indices for the matrix $n_H = 3.3156$, and the holes (the $n_{\rm layer} \to 1$ limit), $n_{\rm eff,holes} = 2.81$. This approach gives too high $n_{\rm eff}$ values, and consequently underestimates the prism's index step $\Delta n$. The reason for the high $n_{\rm eff,holes}$ of 2.81 is the heavily modified fundamental mode profile [see Fig. 8(c)], allowed by the rather thick remaining III–V (top) and Si (bottom) layers. As holes occupy 10–15% of the structure, it is more physical to consider that the field remains vertically nearly unchanged. We thus use a perturbation approach and apply a (v′ $\to$ h) homogenization, trying to guess the phase index of the 'rigid field' illustrated in Fig. 8(b) when it goes through the holes in Fig. 8(c), not having a modified profile. This amounts to extrapolate the slope of Fig. 8(a) to $n_{\rm layer} = n_{\rm air} = 1$. For $n_{\rm layer}$ values close to 3.5, the slope $\partial n_{\rm eff}/\partial n_{\rm layer}$ reflects the impact of the modified index by $\delta n = (3.5 - n_{\rm layer})$ with a nearly identical field. The extrapolation reads: $n_H - n_{\rm eff,holes} = (n_{\rm Si} - n_{\rm air}) \times \partial n_{\rm eff}/\partial n_{\rm layer}$ and gives $n_{\rm eff,holes} = 2.05$. We finish by a (h) step using $n_{\rm eff,holes} = 2.05$ for holes in a Si matrix of index $n_{\rm Si} = 3.5$. The resulting $\Delta n$ values reported in Table III match very well the 3D Bloch mode calculation $\Delta n$(3D).

## REFERENCES


[1] J. K. Doylend and A. P. Knights, "The evolution of silicon photonics as an enabling technology for optical interconnection," *Laser Photon. Rev.*, vol. 6, no. 4, pp. 504–525, 2012.

[2] G. Roelkens, L. Liu, D. Liang, R. Jones, A. Fang, B. Koch, and J. Bowers "III-V/silicon photonics for on-chip and inter-chip optical interconnects," *Laser Photon. Rev.*, vol. 4, no. 6, pp. 751–779.

[3] A. Talneau, C. Roblin, A. Itawi, O. Mauguin, L. Largeau, G. Beaudouin, I. Sagnes, G. Patriarche, C. Pang, and H. Benisty, "Atomic-plane-thick reconstruction across the interface during heteroepitaxial bonding of InP-clad quantum wells on silicon," *Appl. Phys. Lett.*, vol. 102, no. 21, pp. 212101–1– 212101-4, 2013.

[4] C. X. Pang and H. Benisty, "Nanostructured silicon geometries for directly bonded hybrid III–V-silicon active devices," *Photon. Nanostruct.-Fundam. Appl.*, vol. 11, no. 2, pp. 145–156, 2013.

[5] D Labilloy, H. Benisty, C. Weisbuch, T. F. Krauss, R. Houdré, and U. Oesterle, "Use of guided spontaneous emission of a semiconductor to probe the optical properties of two-dimensional photonic crystals," *Appl. Phys. Lett.*, vol. 71, no. 6, pp. 738–740, 1997.

[6] A. Talneau, C. Roblin, A. Itawi, O. Mauguin, L. Largeau, G. Beaudouin, I. Sagnes, and G. Patriarche, "Atomic-plane-thick reconstruction across the interface during heteroepitaxial bonding of InP-clad quantum wells to Si," in *Proc. Int. Conf. IEEE Indium Phosphide Related Mater.*, pp. 130–132, 2012, pp. 130–132.

[7] K. Pantzas, G. Patriarche, E. Le Bourhis, D. Troadec, A. Itawi, G. Beaudoin, I. Sagnes, and A. Talneau, "Evaluation of the surface bonding energy of an InP membrane bonded oxide-free to Si using instrumented nanoindentation," *Appl. Phys. Lett.*, vol. 103, no. 8, p. 081901, 2013.

[8] A. W. Fang, H. Park, Y. H. Kuo, R. Jones, O. Cohen, D. Liang, O. Raday, M. N. Sysak, M. J. Paniccia, and J. E. Bowers, "Hybrid silicon evanescent devices," *Mater. Today*, vol. 10, no. 7, pp. 28–35, 2007.

[9] S. Keyvaninia, S., Verstuyft, S. F. Lelarge, G. H. Duan, S. Messaoudene, J. M. Fedeli, E. J. Geluk, T. D. Vries, B. Smalbrugge, J. Bolk, M. K. Smit, D. V. Thourhout, and G. Roelkens, "Heterogeneously integrated III-V/Si single mode lasers based on a MMI-ring configuration and triplet-ring reflectors," *Proc. SPIE*, vol. 8767, p. 87670N, 2013.

[10] C. Pang, H. Benisty, M. Besbes, X. Pommarede, and A. Talneau, "Oxide-free InP-on-Silicon-on-Insulator nanopatterned waveguides: propagation losses assessment through end-fire and internal probe measurements," *J. Light w. Technol.* vol. 32, no. 6, pp. 1048–1053, Mar. 2014.

[11] D. Labilloy, H. Benisty, C. Weisbuch, T. F. Krauss, D. Cassagne, C. Jouanin, C. R. Houdré, U. Oesterle, and V. Bardinal, "Diffraction efficiency and guided light control by two-dimensional photonic-bandgap lattices," *IEEE J. Quantum Electron.*, vol. 35, no. 7, pp. 1045–1052, Jul. 1999.

[12] C. J. M. Smith, H. Benisty, S. Olivier, M. Rattier, C. Weisbuch, T. F. Krauss, R. M. De La Rue, R. Houdré, and U. Oesterle, "Low-loss channel waveguides with two-dimensional photonic crystal boundaries," *Appl. Phys. Lett.*, vol. 77, no. 18, pp. 2813–2815, 2000.

[13] E. Silberstein, P. Lalanne, J. P. Hugonin, and Q. Cao, "Use of grating theories in integrated optics," *JOSA A*, vol. 18, no. 11, pp. 2865–2875, 2001.

[14] Q. Cao, P. Lalanne, and J. P. Hugonin, "Stable and efficient Bloch-mode computational method for one-dimensional grating waveguides," *JOSA A*, vol. 19, no. 2, pp. 335–338, 2002.

[15] N. Le Thomas, H. Zhang, J. Jágerská, V. Zabelin, V. R. Houdré, I. Sagnes, and A. Talneau, "Light transport regimes in slow light photonic crystal waveguides," *Phys. Rev. B*, vol. 80, no. 12, p. 125332, 2009.